

Cite this: *RSC Adv.*, 2014, 4, 64608

Redox-driven atomic-scale changes in mixed catalysts: $\text{VO}_x/\text{WO}_x/\alpha\text{-TiO}_2$ (110)[†]

 Z. Feng,^{‡ab} M. E. McBriarty,^{‡a} A. U. Mane,^c J. Lu,^c P. C. Stair,^d J. W. Elam^c
and M. J. Bedzyk^{*ae}

X-ray studies of vanadium–tungsten mixed-monolayer-oxide catalysts grown on the rutile $\alpha\text{-TiO}_2$ (110) single crystal surface show redox behavior not observed for lone supported vanadium or tungsten oxides. Two cases are presented: sub-monolayer (sub-ML) vanadium oxide (vanadia) grown on ML tungsten oxide and ML vanadia grown on sub-ML tungsten oxide. The X-ray standing wave (XSW) and X-ray photoelectron spectroscopy (XPS) observations for both cases show coverage-dependent reversible redox-induced atomic-scale structural and chemical state changes. Atomic force microscopy shows that the mixed VO_x/WO_x overlayers have a conformal film-like structure in the as-deposited state. XSW analysis in light of XPS reveals that the V and W cations that are uncorrelated with the substrate lattice play an important role in catalytic redox reactions. Distinct differences in the redox-induced changes for these two mixed catalysts result from tuning the ratio of V to W, and relationships are drawn between the catalyst composition, structure, and chemistry. Comparison of these V–W mixed cases and the corresponding unmixed cases reveals a synergistic effect in which the reduction of W can be significantly enhanced by the addition of V.

Received 8th October 2014
Accepted 20th November 2014

DOI: 10.1039/c4ra14140g

www.rsc.org/advances

1. Introduction

Metals and metal oxides deposited on oxide supports are widely used for many applications, such as gas sensors,¹ electrical and optical switching devices,² and heterogeneous catalysts.^{3,4} Catalytic applications include petroleum refining, selective catalytic reduction (SCR) of automotive and industrial NO_x emissions, and hydrogenation of carbon monoxide to methanol.⁵ Such catalysts are typically composed of supported noble metals (Pd, Pt) or transition metals (V, Nb, Cr, Mo, W, Re) and their oxides.^{6–9} The geometric and electronic structure of the metal or metal oxide on the support and of the interface with the oxide support under reaction conditions controls the activity and selectivity of these catalysts.^{10,11} Consequently, a substantial worldwide effort has been devoted to elucidate and

understand this relationship between structure, activity, and selectivity.

Among catalytic materials, supported vanadium oxide (vanadia) and tungsten oxide have received much attention due to their importance as industrial catalysts. Although progress has been made to understand the structures, individually, of vanadia or tungsten oxide on oxide single crystals^{12–14} and how they respond to chemical reactions,^{15–19} much less is known about the structure and chemistry of supported mixed oxides. It is anticipated that interactions between the oxides will alter their response to reaction conditions. Since the atomic structure of the catalyst affects its performance, the ability to predict the structure of the supported oxide would have an enormous impact on our fundamental understanding of catalytic chemistry at the atomic level. Moreover, TiO_2 -supported $\text{V}_2\text{O}_5\text{-WO}_3$ is the main catalyst for industrial NO_x SCR processes and many other reactions.^{20–24} Therefore an understanding of the relationship between atomic-scale structure and catalytic chemistry for this system under reaction conditions could lead to improved catalyst performance and ultimately reduce the environmental impact of industrial processes.

We approach this challenge by using the tools of surface and interface science, including X-ray standing waves (XSW)²⁵ and X-ray photoelectron spectroscopy (XPS). The XSW technique is used to probe the element-specific structure of an ad-layer on a single crystal surface with sub-Å resolution.^{26–30} Dynamical Bragg diffraction from a single crystal substrate causes an XSW to be generated with a period equal to the d -spacing d_{hkl} of the

^aDepartment of Materials Science and Engineering, Northwestern University, Evanston, IL, 60208, USA

^bChemical Sciences and Engineering Division, Argonne National Laboratory, Lemont, IL, 60439, USA

^cEnergy Systems Division, Argonne National Laboratory, Lemont, IL, 60439, USA

^dDepartment of Chemistry, Northwestern University, Evanston, IL, 60208, USA

^eDepartment of Physics and Astronomy, Northwestern University, Evanston, IL, 60208, USA. E-mail: bedzyk@northwestern.edu

[†] Electronic supplementary information (ESI) available: Details about the material growth, AFM, XPS, and XSW characterizations. See DOI: 10.1039/c4ra14140g

[‡] Equal contribution and cofirst authors.

diffracting crystal planes. Rotating the crystal through an $H = hkl$ Bragg condition causes the XSW phase to shift inward by $\frac{1}{2}d_H$. This results in a lattice-position-dependent modulation in the X-ray fluorescence (XRF) yield for a given atomic species. Analysis of this modulation directly determines a model-independent Fourier amplitude f_H and phase P_H for that atom's distribution.^{31,32} A Fourier summation with this set of XSW measured Fourier components (and their symmetry equivalents) produces a model-independent 3D atomic distribution projected onto the substrate primitive unit cell.^{33–36} Recently we have demonstrated that XSW is a unique *in situ* tool to understand the atomic-scale behavior of oxide-supported planar model catalysts during various chemical reactions.^{12,15–17,37–40} In this work, we use XSW to observe chemical state-dependent changes in the V and W geometry and surface site occupancy. We also determine the fraction of atoms that are uncorrelated to the substrate lattice. XSW analysis in combination with XPS results allows us to associate chemical state changes of ad-layer atomic species with structural changes.

Previous studies have shown that monolayer (ML) and sub-ML vanadia supported on TiO_2 and other oxides can go through both structural and chemical state changes during reduction–oxidation (redox) reaction cycles.^{2,10,37,38,41,42} In contrast, ML and sub-ML tungsten oxide films supported on oxide substrates tend to be immobile and irreducible from the W^{6+} state under similar catalytic conditions.^{12,43–45} A notable exception is for sub-ML tungsten oxide on the reducible substrate $\alpha\text{-Fe}_2\text{O}_3$ (0001), for which a reduction to W^{5+} and corresponding redox-reversible structural shifts are observed.^{15,19} If the oxide supporting a surface tungsten species can affect its structural and chemical behavior, then other nearby surface species such as oxo-vanadium may have similar effects on the tungsten species. By studying the effect of vanadia on the W surface site configuration and oxidation state (and *vice versa*), the structural and chemical factors which are responsible for V–W catalytic synergy may be clarified. To this end, we atomically engineered vanadia on top of tungsten oxide over a single crystal $\alpha\text{-TiO}_2$ (110) surface. The single crystal $\alpha\text{-TiO}_2$ serves the dual role of the chemically active catalyst support as well as the near-perfect atomic lattice required for XSW measurements.

Herein, we report the synthesis by atomic layer deposition (ALD) and structural transformations of two mixed oxide catalysts supported on $\alpha\text{-TiO}_2$ (110): sub-ML vanadia on ML tungsten oxide and ML vanadia on sub-ML tungsten oxide. *In situ* XSW atomic imaging is combined with *ex situ* XPS and atomic-force microscopy (AFM) to study the geometric and electronic structures of the mixed catalysts as they undergo reduction–oxidation (redox) reactions. We also draw comparisons between these results and our earlier studies of single-component ALD-grown ML or sub-ML films of VO_x or WO_x on $\alpha\text{-TiO}_2$ (110).^{12,37–39}

2. Experimental

2.1 Sample preparation

Polished rutile $\alpha\text{-TiO}_2$ (110) ($10 \times 10 \times 1 \text{ mm}^3$) single crystal substrates were annealed in oxygen at 900 °C for 1 h to obtain

atomically flat surfaces. To grow mixed catalysts by ALD at 200 °C, tungsten oxide was deposited first, followed by vanadium oxide. Tungsten hexafluoride (WF_6) and vanadyl oxy-triisopropoxide, ($\text{VO}_4(\text{C}_3\text{H}_7)_3$, VOTP), were used as the metal precursors for the W and V ALD, respectively. For one set of samples, the substrates were ALD-coated with 2 W cycles, followed by 1 V cycle, and for the other set, the substrates were coated with 1 W cycle and then 2 V cycles (see ESI† for details).

2.2 XSW, XPS and AFM measurements

After ALD growth, the samples were removed from the reactor and mounted on a 5-circle diffractometer for XSW and XRF analysis at the Advanced Photon Source (APS) 5ID-C station. The samples were placed on a ceramic heating stage inside a beryllium dome gas reaction cell that was mounted on the diffractometer (see Fig. S2†). The V and W coverages were determined by XRF and quantified by comparison to a calibrated standard sample. For the sample with 2 W cycles followed by 1 V cycle, the W and V coverages were $\Theta = 1.2 \text{ ML}$ and 0.7 ML , respectively; this sample will be referred to as sub-VW. For the sample with 1 W cycle followed by 2 V cycles, the W and V coverages were $\Theta = 0.6 \text{ ML}$ and 1.1 ML , respectively; this sample will be referred to as ML-VW. For the single crystal experiments reported here, 1 ML is defined as the area density of Ti atoms in the TiO (110) plane of TiO_2 , or 10.4 atoms per nm^2 . The oxidized and reduced surfaces were prepared inside the Be dome by annealing at 400 °C for 30 min in O_2 and 2% H_2 in helium, respectively, at 760 torr. The *in situ* XSW measurements were taken at room temperature after each processing step, starting with the as-deposited (AD) surface, then the oxidized (OX), then the reduced (RD), and finally the re-oxidized (OX2) surface. The OX2 measurement was used to check for redox reversibility.

The surface morphology of the $\alpha\text{-TiO}_2$ (110) single crystal substrates was examined by AFM under ambient conditions after the initial oxygen annealing treatment and after the ALD growth. *Ex situ* XP spectra were taken after the OX, RD, and OX2 processing steps. Samples were briefly exposed to air during transport from the reactor to the ultra-high vacuum (UHV) XPS instrument. To check the surface stability under ambient conditions, the $\text{OX} \rightarrow \text{RD} \rightarrow \text{OX2}$ XSW measurements were repeated after a month of storage in a dry desiccator box. Similar f_H and P_H values were found, indicating that the V and W atomic structures are stable in air. We also checked the XSW results for an air-exposed sample after one of the redox steps to confirm the stability of our results. Thus, the *ex situ* XPS and AFM results can be used to describe the surface conditions for *in situ* XSW measurements.

3. Results and discussion

AFM images of the $\alpha\text{-TiO}_2$ (110) substrate surfaces before ALD deposition show large, atomically flat terraces separated by atomic steps of 3.3 Å, which is the d -spacing of $\alpha\text{-TiO}_2$ (110). After ALD, the atomic steps are still clearly visible, indicating

conformal VO_x and WO_x film formation by ALD (see AFM images in Fig. S1 in the ESI†).

Fig. 1 shows the XPS analyses for the two cases at each redox processing step. The measured spectra for the OX2 surface (not shown) matched that of OX, indicating redox reversibility of the chemical states of the surface cations. The assignment of oxidation states for V and W are based on published V 2p_{3/2} and W 4f binding energies (BE)^{12,46–48} and the binding energy differences (BED)⁴⁶ of V 2p_{3/2} to O 1s that are listed in Table S1.† For the as-deposited and oxidized surfaces in both the sub-VW and ML-VW cases, V and W are completely oxidized to V⁵⁺ and W⁶⁺, respectively. We also found V and W to be completely oxidized for unmixed sub-ML and ML cases on α -TiO₂ (110).^{12,37–39} However, as can be seen in Table 1, the reduced surfaces show chemical states that vary with increasing V and/or W coverages. For example, the only case in which W was found to be reducible was sub-VW with 1.2 ML of W. Mixed or unmixed, V was found to be reducible for all coverages examined with an increased percentage reduced as the V coverage is increased. For coverages $\Theta < 1$ ML, V was reduced to 3+, whereas V was reduced to 4+ for $\Theta > 1$ ML. Note that the O 1s peak is broader in the RD state as compared to the OX state, suggesting that O exhibits a variety of chemical states that do not correspond to stoichiometric WO₃.⁴⁸ The O 1s peak does not shift significantly for different stoichiometries of vanadium oxide, and the Ti peak does not shift, indicating that TiO₂ is stoichiometric and not reduced substantially under these conditions.⁴⁹ Therefore, we consider three contributions with three

Table 1 XPS determination of reduced chemical states of ALD V and/or W on α -TiO₂ (110) single crystal surfaces for the two mixed cases of this study, the unmixed 1.0 monolayer (ML) W case described in ESI, and other unmixed cases^{12,37–39} published earlier. For all seven cases XPS shows that the oxidized surfaces have 100% V⁵⁺ and 100% W⁶⁺. When these surfaces are reduced, the tabulated percentages of cations reduce to the tabulated chemical states. The remaining percentages are unchanged from V⁵⁺ and W⁶⁺. A coverage of $\Theta = 1$ ML corresponds to 10.4 atoms per nm²

W Θ	V Θ				
	0 ML V	0.7 ML V	1.1 ML V	1.5 ML V	2.0 ML V
0 ML W		25% V ³⁺		61% V ⁴⁺	100% V ⁴⁺
0.4 ML W	No change				
0.6 ML W			33% V ⁴⁺		
1.0 ML W	No change				
1.2 ML W		56% V ³⁺ 11% W ⁴⁺ 35% W ⁵⁺			

distinct chemical shifts to the O 1s peak. BE = 530.0 eV is assigned to VO_x, TiO₂, and stoichiometric WO₃ (with W⁶⁺ cation centers), BE = 531.5 is assigned to sub-stoichiometric WO_x (with a mixture of W⁵⁺ and W⁴⁺ cation centers), and BE = 532.5 eV is assigned to hydroxyl groups.

As seen in Table 1 the chemical state changes of sub-ML and ML V in mixed catalysts during redox reactions are consistent with our previous studies of pure VO_x (without WO_x) grown by ALD on α -TiO₂ (110). For pure VO_x, the sub-ML V oxidation state changes from V⁵⁺ in the OX state to a mix of V³⁺ and V⁵⁺ in the RD state,³⁷ and the 2 ML V changes from V⁵⁺ in the OX state to V⁴⁺ in the RD state.³⁹ Our previous study of pure sub-ML WO_x showed no chemical state change from W⁶⁺ in the redox reaction, similar to the result reported herein for the mixed catalyst ML-VW case.¹² The pure 1.0 ML WO_x case (see ESI†) also shows no chemical state change from W⁶⁺ in the redox reaction, unlike the chemical state changes observed herein for 1.2 ML W in the sub-VW case.

Fig. 2 shows a representative set of *in situ* XSW data and analytical fits after the OX, RD, and OX2 steps for the sub-VW and ML-VW cases. The changes in the V XSW data through an OX → RD → OX2 cycle indicate reversible redox-induced V atomic distribution changes in both cases; likewise, W shows redox-reversible shifts in the sub-VW case. For W in the ML-VW case, however, no change in the W structural distribution is observed. The XSW-measured Fourier amplitudes and phases (listed in Table S2†) are then summed (eqn S1†) to create model-independent density maps^{33–35} for the V and W cations. Fig. 3 and 4 show these 3D atomic density maps at the OX and RD states for the ML-VW and sub-VW cases, respectively. The “hot spots” in the maps are the V or W density maxima. Fourier inversion causes these maps to inherit the periodicity of the substrate primitive unit cell. Since W in ML-VW does not undergo structural changes during redox reactions, there is only one W density map shown in Fig. 3. As illustrated in Fig. 3d these density maps are referenced to a α -TiO₂ (110) surface unit

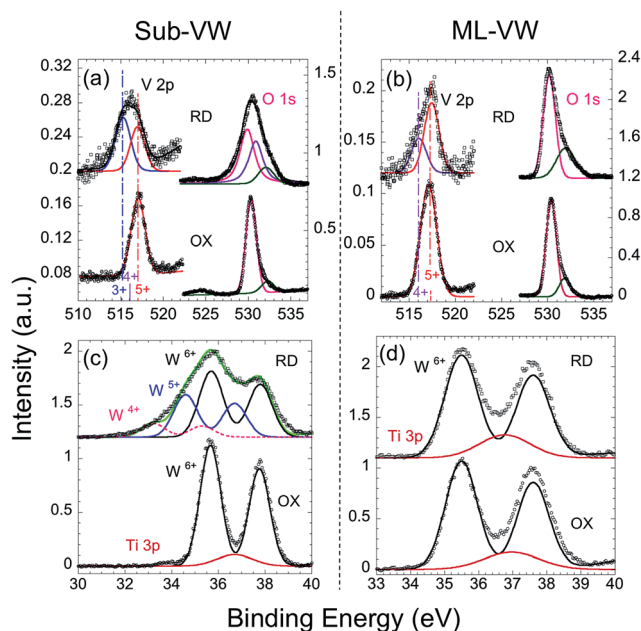


Fig. 1 XP spectra of VO_x/WO_x/ α -TiO₂ (110) mixed catalysts in oxidized (OX) and reduced (RD) states. XP regions are shown corresponding to (a and b) V 2p_{3/2} and O 1s peaks and (c and d) W 4f_{7/2} and 4f_{5/2} doublet peaks and the Ti 3p peak for (a and c) the sub-VW case of 0.7 ML VO_x/1.2 ML WO_x/ α -TiO₂ (110) and (b and d) the ML-VW case of 1.1 ML VO_x/0.6 ML WO_x/ α -TiO₂ (110). XPS was collected at a 45° electron emission angle. The peak fit results are listed in Table 1.

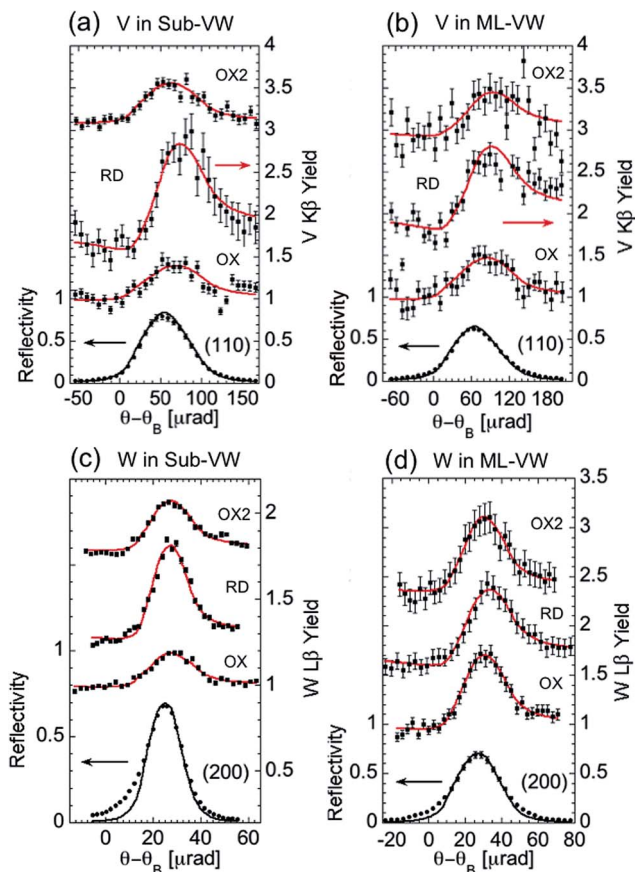


Fig. 2 Representative XSW data and fits for two mixed catalyst samples at the (a and b) (110) surface normal and (c and d) (200) off-normal directions showing (a and b) vanadium and (c and d) tungsten structural changes for the oxidized (OX), reduced (RD), and re-oxidized (OX2) stages of a redox reaction cycle. Results for OX2 match well with those for OX, indicating that structural changes are reversible. Sub-VW (a and c) denotes the sample with 0.7 ML vanadia deposited on top of 1.2 ML tungsten oxide, and ML-VW (b and d) denotes the sample with 1.1 ML vanadia deposited on top of 0.6 ML tungsten oxide.

cell, which is a non-primitive 3D unit cell chosen for convenience to have a (110) surface as one of the unit-cell faces.^{12,37,39} In this unit cell, there are two symmetry-inequivalent Ti sites, namely atop (AT) and bridging (BR) sites, which are depicted as solid (AT) and open (BR) blue circles. V and W cations in the sub-VW case clearly prefer the BR adsorption sites on the rutile (110) surface, while V and W cations in the ML-VW case are distributed equally between AT and BR sites. Some displacements in the surface normal direction are observed between the measured “hot spots” and the bulk-like Ti sites. The W density map of the 0.6 ML WO_x in the ML-VW mixed catalyst is similar to that of pure 1.0 ML W on $\alpha\text{-TiO}_2$ (110) (see ESI†).

Since the XSW model-independent V and W atomic maps (Fig. 3 and 4) only exhibit “hot spots” at the AT and BR sites, we can determine the structural parameters for these two sites by performing a least-squares global fit to the set of measured f_H and P_H values for each chemical condition. In this model the H^{th} Fourier component for the V or W atomic distribution is described as,³⁰

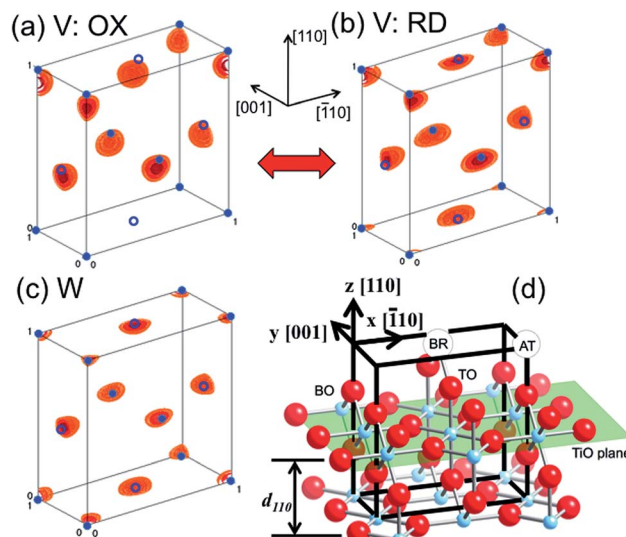


Fig. 3 XSW measured atomic density maps of 1.1 ML vanadia and 0.6 ML tungsten oxide deposited on $\alpha\text{-TiO}_2$ (110) (ML-VW case). Each map is projected onto the $\alpha\text{-TiO}_2$ unit cell, where symmetry-inequivalent AT (filled blue circles) and BR (open blue circles) bulk-like Ti sites are shown. (a) and (b) show the V cation density maps plotted in the reference unit cell in oxidized (OX) and reduced (RD) surface conditions, respectively; (c) is the W cation density map, which does not change through the redox cycle; and (d) shows a ball-and-stick model of the $\alpha\text{-TiO}_2$ (110) surface termination with oxygen atoms in red, Ti in blue, and cation adsorption sites in white (atop (AT), bridge (BR)). The non-primitive unit cell, outlined with heavy black lines, is referred to as the (110) surface unit cell and is used as the reference to locate V and W cation positions in XSW 3D atomic density maps.

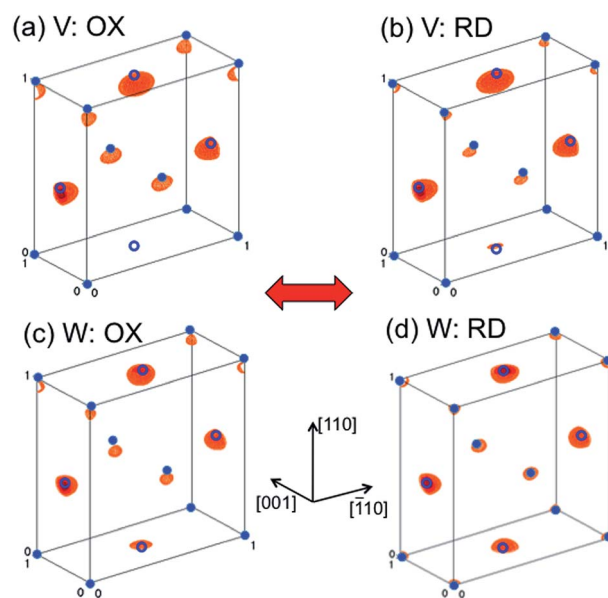


Fig. 4 Atomic density maps of 0.7 ML vanadia and 1.2 ML tungsten oxide deposited on $\alpha\text{-TiO}_2$ (110) (sub-VW case). (a and b) V and (c and d) W cation density maps are plotted in the (110) surface unit cell for oxidized (OX) and reduced (RD) surface conditions. Bulk-like Ti sites are shown as blue circles, in the same scheme as used in Fig. 3.

$$F_H = f_H \exp(2\pi i P_H) = \exp(-2\pi^2 \sigma^2 / d_H^2) \times [c_{AT} \exp(2\pi i \mathbf{H} \cdot \mathbf{r}_{AT}) + c_{BR} \exp(2\pi i \mathbf{H} \cdot \mathbf{r}_{BR})], \quad (1)$$

where c_X denotes the V or W cation occupation fraction at the AT and BR sites with positions $\mathbf{r}_{AT} = (0, 0, z_{AT})$ and $\mathbf{r}_{BR} = (1/2, 1/2, z_{BR})$, with z_X denoting the cations' heights in the [110] direction above the bulk-like TiO plane. The fit parameter σ accounts for an isotropic time-averaged Gaussian displacement field of the cations about the two sites. d_H is the diffraction plane spacing. Tables 2 and 3 list the best-fit determined results of the cation occupation fractions and adsorption heights for sub-VW and ML-VW samples, respectively. As a consistency check, the measured Fourier components are compared with the calculated values, f_H^C and P_H^C , that would have been observed if V and W occupied sites as dictated by this best-fit model (Tables S2 and S3†). Furthermore, Tables 2 and 3 show that the correlated fractions, c_{BR} and c_{AT} , do not change through the redox reaction cycle for V and W in the sub-VW case and for W in the ML-VW case. The total correlated fraction, $\sum c = c_{BR} + c_{AT}$, is of course also constant. Thus, for these cases there is minimal redox-induced atomic transfer between the BR and AT sites. The remaining fraction of cations ($1 - \sum c$) are uncorrelated to the substrate lattice and cannot be described further by the XSW technique. From eqn (1) we define the uncorrelated component as that in which the Fourier amplitudes $f_H = 0$ for all $H = hkl$, except $H = 0$.

In the discussion below, we partition the surface cations into three different phases: a rutile-like correlated layer; a monolayer phase which is conformal to the crystal surface but not correlated with the rutile structure; and a 3-dimensional phase consisting of nanoparticles on the surface, as is visible in Fig. S1 in the ESI.† Only the correlated layer is structurally visible by the XSW technique, and the total coverage of this phase is quantified as the sum of coherent fractions of V and W ($\sum c = c_{BR} + c_{AT}$) multiplied by the total coverage of each respective species. The average positions of atoms in the AT and BR sites are also

Table 2 Sub-VW parameters determined from the fit of the two-site model (eqn (1)) to the XSW measured V and W Fourier components listed in Table S2. The c_X values are the fractions of V and W atoms at X = BR or AT sites. The corresponding ML coverage for each site ($\theta_X = c_X \theta_{\text{total}}$) is shown in italic below the c_X values. z_X is the height above the bulk TiO atomic plane in the (110) direction. For comparison, Ti in bulk α -TiO₂ has $z_{BR} = z_{AT} = d_{110} = 3.25$ Å

Surface	c_{BR}	c_{AT}	$\sum c$	z_{BR} (Å)	z_{AT} (Å)	σ (Å)
0.7 ML V						
OX	0.38(6)	0.14(3)	0.52(7)	3.09(3)	2.75(9)	0.15(9)
	<i>0.27 ML</i>	<i>0.10 ML</i>	<i>0.36 ML</i>			
RD	0.40(7)	0.09(5)	0.49(9)	3.12(3)	3.22(9)	0.21(8)
	<i>0.28 ML</i>	<i>0.06 ML</i>	<i>0.34 ML</i>			
1.2 ML W						
OX	0.26(1)	0.10(1)	0.36(1)	3.19(2)	2.98(3)	0.29(1)
	<i>0.31 ML</i>	<i>0.12 ML</i>	<i>0.43 ML</i>			
RD	0.27(1)	0.09(1)	0.36(1)	3.18(2)	3.19(2)	0.32(1)
	<i>0.32 ML</i>	<i>0.11 ML</i>	<i>0.43 ML</i>			

Table 3 ML-VW XSW parameters, same as described for Table 2

Surface	c_{BR}	c_{AT}	$\sum c$	z_{BR} (Å)	z_{AT} (Å)	σ (Å)
1.1 ML V						
OX	0.20(4)	0.28(9)	0.5(1)	3.04(9)	3.11(9)	0.16(9)
	<i>0.22 ML</i>	<i>0.3 ML</i>	<i>0.5 ML</i>			
RD	0.35(9)	0.38(9)	0.7(1)	3.41(6)	2.96(6)	0.18(9)
	<i>0.4 ML</i>	<i>0.4 ML</i>	<i>0.8 ML</i>			
0.6 ML W						
OX	0.30(2)	0.21(2)	0.51(3)	3.31(4)	3.38(2)	0.33(2)
	<i>0.18 ML</i>	<i>0.13 ML</i>	<i>0.31 ML</i>			
RD	0.25(2)	0.21(1)	0.46(2)	3.29(2)	3.37(2)	0.16(3)
	<i>0.15 ML</i>	<i>0.13 ML</i>	<i>0.28 ML</i>			

precisely quantified. The other two phases consist of the remaining fraction of cations ($1 - \sum c$) multiplied by the total coverage. We note that one compact, correlated rutile-like monolayer consists of 0.5 ML cations in the AT site and 0.5 ML occupying BR; any higher cation occupation value implies that there is more than one coherent cation monolayer.

To make sense of the differences in the correlated cation heights z_{AT} and z_{BR} observed for some samples, we first consider the relaxed structure of the bare α -TiO₂ (110) single crystal surface. As the AT and BR sites sit exclusively along separate lines perpendicular to the (110) plane, the positions of near-surface substrate cations at positions along these lines could affect the positions of surface atoms above them. The Ti atom in the AT site closest to the surface of a clean α -TiO₂ (110) crystal has been observed to shift downward by 0.16–0.19 Å from a bulk-like position, whereas the Ti atom in topmost BR site shifts upward by 0.12–0.25 Å.⁵⁰ The correlated W positions in our previous work on 0.4 ML WO_x/ α -TiO₂ (110) reflect the cation structure of the underlying substrate: the BR atom sits at a z -height of about 0.3 Å above that of the AT atom.¹² Similar behavior is observed for W in the sub-VW sample, although the AT and BR W positions are about 0.3–0.4 Å lower than for the 0.4 ML W case. This does not follow, however, for the correlated fraction of W on the ML-VW sample, in which the z_{AT} coherent position is slightly higher than z_{BR} . We recall that of the 0.4 ML W in the previously reported case, about 0.3 ML is correlated with the substrate lattice, equally occupying the AT and BR sites. The total correlated coverage of W and distribution between AT and BR sites are similar between the 0.4 ML W sample and the ML-VW sample. We note that the AT and BR components of the 0.4–0.5 ML of correlated W in the 1.0 ML WO_x/ α -TiO₂ (110) case appear to be coplanar, both sitting 0.1 Å above the rutile-like cation positions (see Table S5 in the ESI†).

To our knowledge, epitaxial growth of WO₃ on the α -TiO₂ (110) single crystal surface has not been reported. This is likely due to the large mismatch of the α -TiO₂ (110) surface cell ($d_{110} = 6.50$ Å, $d_{001} = 2.96$ Å) with WO₃, which has a pseudo-cubic monoclinic⁵¹ or triclinic⁵² unit cell with lattice parameters between 7.3 and 7.7 Å. Among all cases we have studied for this system, including 0.38 ML WO_x/ α -TiO₂,¹² the total correlated W coverage never exceeds 0.5 ML. This further suggests the

inability of the rutile lattice to accommodate a complete monolayer of W^{6+} . As the cations in rutile have a nominal 4+ charge, a coherent monolayer of W^{6+} would require charge balancing from additional ligands (which may be unfavorable due to anion–anion repulsion) or by cationic vacancies. Detailed structures of W_3O_9 clusters deposited on α - TiO_2 (110) at low coverages have recently been reported⁵³ which provide clues to the W – TiO_2 interaction. For these structures, W tends to adsorb more closely to AT than BR sites, although the preference shifts towards BR sites if the substrate is slightly reduced,⁵⁴ indicating the subtle influence of surface conditions on the preferred adsorption site of W.

Considering the correlated coverage values in monolayer units provided in Table 3 for the ML-VW sample, the total occupation of AT sites by V and W ranges from 0.4–0.5 ML between the OX and RD conditions, and likewise for BR, 0.4–0.6 ML, indicating that more than one layer of correlated atoms may be stacked on the surface. While a similar multi-layer case has been observed for 2.0 ML VO_x/α - TiO_2 (110),³⁹ the assignment is not straightforward due to modular ambiguities inherent in XSW analysis.

From the above arguments, we propose that the correlated cations in the oxidized case constitute a “pseudo-rutile” mixed oxide layer consisting of W^{6+} and V^{5+} . Cation defects inside the ultrathin film must accommodate the O^{2-} ligands necessary to coordinate the higher-valence W^{6+} and V^{5+} cations. This implies that the coverage corresponding to one layer of this pseudo-rutile structure must contain less than 1 ML of coherently ordered cations, or more specifically, that one layer of AT or BR occupation must contain less than 0.5 ML of V and W combined. Cations in the first epitaxial layer may occupy positions slightly above the bulk-like rutile sites, as in previous work on V or W alone. Cations in the second layer may “sink” into the unoccupied sites below, resulting in a lower-than-expected cation position as measured by XSW. The average modulo- d_{110} position measured by XSW may therefore be lower than the bulk-like rutile position. Shifts in the correlated cation position occur in response to changes in the structure of uncorrelated phases in their vicinity.

In our previous work on >1 ML VO_x/α - TiO_2 (110), no correlated V^{5+} was observed, whereas for different coverages of WO_x/α - TiO_2 (110), we always find correlated W^{6+} . Our evidence shows that W^{6+} on this surface stabilizes V^{5+} in a pseudo-rutile phase. We note that bulk rutile or rutile-like (V and W) O_2 phases have been observed, although these are characterized as reduced phases consisting of V^{3+} , W^{4+} , and W^{6+} .⁵⁵ Pentavalent cations, which are not found in binary rutile structures, can exist in ternary rutile-like oxides along with lower-valent cations. Examples of these rutile-like structures include $CrVO_4$ and several arsenates, tantalates, and niobates.⁵⁶ While these structures must contain divalent or trivalent co-cations, it may be possible to stabilize a defect-rich ultrathin pseudo-rutile phase of higher-valent cations at an interface. We hypothesize that the lower energy of an epitaxial interface with the underlying α - TiO_2 (110) surface outweighs the cation vacancy formation energy of this pseudo-rutile structure, allowing V^{5+} and W^{6+} to be accommodated in an ultrathin $V_{1-x}W_{1-y}O_4$ pseudo-rutile

phase. Uncertainties in the XSW technique and the possibility for non-bulk-like coordination at the interfaces of the ultrathin film preclude a precise quantification of the stoichiometry of this pseudo-rutile phase. However, this pseudo-rutile model accounts very well for the structures unambiguously observed through XSW analysis.

The pseudo-rutile model assists in the interpretation of the observed redox-reversible structural changes. In the ML-VW case, the W component changes neither chemically nor structurally. However, roughly 40% of the V cations, which are uncorrelated in the oxidized condition, move into sites that are correlated to the substrate lattice upon surface reduction. This is consistent with our previous study of 2.0 ML VO_x on α - TiO_2 (110), in which V cations go through a redox-reversible change from 100% uncorrelated V^{5+} for the oxidized surface to 66% correlated V^{4+} and 34% uncorrelated V^{5+} for the reduced surface.³⁹ While roughly 70% of V in the reduced ML-VW case is correlated, only 33% V are reduced to the 4+ state from V^{5+} . A shift in the position of V is also observed, with z_{BR} and z_{AT} slightly below the bulk-like cation position of 3.25 Å in the oxidized case but a significant upward displacement of z_{BR} and an insignificant drop in z_{AT} upon reduction. These redox-reversible changes indicate a shift from an uncorrelated V_2O_5 layer to correlated, rutile-like VO_2 , while the pseudo-rutile phase neither reduces nor changes structure. The remaining V remains uncorrelated to the substrate lattice.

In the ML-VW sample, no reduction from W^{6+} is observed. However, for the sub-VW case, XPS (with a 10% uncertainty) shows that surface reduction causes half of the V and half of the W to undergo chemical state changes (see Table 1). Despite this substantial chemical transformation, the correlated fractions and site distributions for both V and W are unchanged. A significant shift occurs in the position of the correlated V and W in the AT sites between oxidation and reduction. However, these components only comprise a small fraction of the total correlated cations and cannot account for the entire oxidation state shift observed; BR sites are strongly preferred by both V and W over AT sites, with a total occupation of 0.6 ML in the BR sites and 0.2 ML in the AT sites. The lack of a significant restructuring of the surface cations implies that the coherent pseudo-rutile phase is largely unchanged by the reaction, and the uncorrelated cations are responsible for the observed reversible chemical state changes for both V and W in the sub-VW sample.

In our previous XSW and theoretical study on 0.7 ML VO_x/α - TiO_2 (110), 25% of V^{5+} reduced to V^{3+} , whereas for the sub-VW sample, 56% of V^{5+} reduces to V^{3+} .³⁷ Theoretical calculations showed that lower-coordinate VO_x species are more likely to reduce to V^{3+} . This behavior is also predicted by simple chemical considerations: the reaction of a H_2 molecule with a vanadyl group coordinating an isolated V^{5+} monomer, which is more likely to be present in a highly dispersed VO_x phase, is a two-electron process which would result in the reduction of V^{5+} to V^{3+} (and oxidation of H_2 to H_2O). However, in an extended phase consisting of bridged V^{5+} species, a H_2 molecule could cause two separate one-electron reduction events, and reduction from V^{5+} to V^{4+} may be expected. Table 1 shows that, as expected, higher coverages of V^{5+} reduce to V^{4+} , whereas lower coverages

reduce to V^{3+} . We conclude that the presence of WO_x in the sub-VW sample helps to disperse VO_x species, improving their reducibility.

The ordering of W cations with or without additional V provides clues towards the correlated pseudo-rutile structure. For the 1.0 ML $WO_x/\alpha-TiO_2$ (110) sample and the 1.2 ML W in the sub-VW case, the total amount of coherent W is about the same (about 0.4–0.5 ML). However, in the presence of V, the correlated W atoms sit substantially lower relative to the rutile lattice (by about 0.15–0.35 Å), and the ratio $c_{BR} : c_{AT}$ is about 3 : 1 in the presence of V vs. 1 : 1 for W only. Both of these differences could be explained by an ordered cation vacancy structure in the pseudo-rutile layer.

Regarding the cation fraction that is not structurally visible to the XSW technique, it is likely that some of the incoherent V has formed a bulk-like, multi-layer V_2O_5 phase. While Raman spectroscopy unambiguously reveals the presence of bulk-like V_2O_5 in catalyst powders,⁵⁷ this method cannot be applied to our two-dimensional single crystal sample surfaces. The threshold of V_2O_5 particle formation in V-containing catalysts is about 8 V nm⁻² on Al_2O_3 supports, below which VO_x exists as a conformal, well-dispersed phase.⁵⁷ Oxide-supported V_2O_5 crystallites are also shown to resist reduction at temperatures lower than 500 °C under similar conditions as our experiments, suggesting that they may not play a role in the reduction–oxidation shifts observed in this work. However, dispersed sub-monolayer VO_x phases begin to reduce at much lower temperatures, reaching a minimum near 4.4 V nm⁻²; it is likely that such a phase is responsible for the redox behavior of the ML-VW sample.

Previous studies of vanadia, tungsten oxide, or V–W mixtures supported on TiO_2 powder have shown that V is much more catalytically active than W for a variety of chemical reactions.^{58–60} With W added to V, however, the catalytic activity is improved.^{24,61} Bertinchamps *et al.* attribute this synergy to the additional Brønsted acid sites provided by W,⁶¹ yielding enhanced catalytic performance for the mixed catalysts over their constituents. Previous studies^{24,61} also show that the performance of V–W mixed catalysts is optimized when the atomic concentration ratio of W to V is greater than 1. This is consistent with our findings: W is reducible when the W : V ratio is about 2 : 1, while W shows no chemical state changes for the opposite ratio. As the structural shift of the correlated W is minimal, we propose that the uncorrelated W is responsible for this chemical behavior. For V–W mixed oxide catalysts supported on TiO_2 powder, X-ray diffraction measurements combined with reactivity experiments^{24,61} indicate that crystalline WO_x improves catalytic activity only slightly, while non-crystalline WO_x , which has a much more catalytically active surface, significantly improves the catalytic properties.⁶¹ In our mixed catalyst studies, the sum of the W and V uncorrelated coverages, $\Theta(1 - \sum c)$, is significantly higher for the sub-VW case (1.1 ML), in which W^{6+} is reducible, than for the ML-VW case (0.84 ML oxidized, 0.65 ML reduced). This suggests a relationship between the catalyst stoichiometry, structure, and reactivity: the addition of tungsten to vanadia in a $\sim 2 : 1$ ratio results in a reactive phase that is uncorrelated with the lattice of

the oxide support. Crystalline WO_x is generally catalytically inactive and thermodynamically stable in the temperature range of our redox reaction, 400 °C,^{58,62} so it is not surprising that chemical state changes of W are only observed for the sub-VW sample, which has a higher uncorrelated fraction of W than the ML-VW sample.

4. Conclusion

For $\alpha-TiO_2$ (110)-supported VO_x - WO_x mixed catalysts, two cases were investigated: 0.7 ML VO_x mixed with 1.2 ML WO_x (sub-VW), and 1.1 ML VO_x mixed with 0.6 ML WO_x (ML-VW). AFM shows that the VO_x and WO_x formed a conformal thin film after atomic layer deposition. XSW analysis shows that through a redox reaction cycle, the amount of correlated V and W in sub-VW and W in ML-VW stay unchanged, with the exception of V in ML-VW. This indicates that uncorrelated V and W nanoparticles and/or non-lattice-like defect sites play an important role during the redox reactions. XPS analysis in light of XSW results suggests that V in both cases, as well as uncorrelated W in the sub-VW case, go through redox-reversible chemical state changes. The V in the ML-VW case shows an uncorrelated–correlated structural transformation, but otherwise no dramatic structural changes are observed. However, the dynamics of uncorrelated V and W in a redox reaction cycle affect nearby correlated V and W, causing variation in their position relative to the substrate. Redox reversibility was observed in this process, demonstrating this work's relevance to real-world catalytic reaction cycles.

Compared with previous studies of WO_x supported by TiO_2 single crystals and powders, the addition of V to W leads to the enhanced chemical state changes due to synergistic effects between the cations, which is consistent with results from powder-supported mixed catalysts. Our studies also reveal that the mixed catalysts show enhanced chemical state shifts as the amount of additional W increases, which we attribute to the increase in the ratio of uncorrelated to correlated catalyst species. This study demonstrates the importance of structurally uncorrelated cations in chemical reactions, which further helps to understand redox-induced changes in catalyst chemical bonding and the role of the supporting oxides in catalytic reactions.

Acknowledgements

This work was supported by the Institute for Catalysis in Energy Processes at Northwestern University (U. S. Department of Energy under contract DE-FG02-03ER15457) and a National Science Foundation Graduate Research Fellowship under Grant no. DGE-0824162 to MEM. This material is based upon work supported as part of the Institute for Atom-efficient Chemical Transformations (IACT), an Energy Frontier Research Center funded by the U. S. Department of Energy, Office of Science, Office of Basic Energy Sciences. Synchrotron X-ray measurements were performed at the Argonne National Laboratory (ANL) Advanced Photon Source, Sector 5 (DND-CAT) and Sector 33. DND-CAT is supported by E. I. duPont de Nemours & Co.,

Northwestern University, The Dow Chemical Co., the State of Illinois through the Department of Commerce and the Board of Education (HECA), and the US National Science Foundation through the MRSEC (NSF Award DMR-1121262). ANL is supported by the US Department of Energy Office under contract DE-AC02-06CH11357. AFM and XPS were carried out at the NIFTI and Keck-II facilities of NUANCE at Northwestern University. The authors are thankful for technical assistance at DND-CAT by Dr Denis Keane and for useful discussions with Dr Chang-Yong Kim and Prof. Kenneth Poeppelmeier.

Notes and references

- V. E. Henrick and P. A. Cox, *The Surface Science of Metal Oxides*, Cambridge University Press, 1996.
- S. Surnev, M. G. Ramsey and F. P. Netzer, *Prog. Surf. Sci.*, 2003, **73**, 117–165.
- K. Hermann and M. Witko, in *The Chemical Physics of Solid Surface: Oxide Surface*, ed. D. P. Woodruff, Elsevier Science, 2001, vol. 9, p. 136.
- B. GrzybowskaSwierkosz and F. Trifiro, *Appl. Catal., A*, 1997, **157**, 1–2.
- B. C. Gates, *Chem. Rev.*, 1995, **95**, 511–522.
- H. J. Freund and G. Pacchioni, *Chem. Soc. Rev.*, 2008, **37**, 2224–2242.
- S. T. Christensen, J. W. Elam, F. A. Rabuffetti, Q. Ma, S. J. Weigand, B. Lee, S. Seifert, P. C. Stair, K. R. Poeppelmeier, M. C. Hersam and M. J. Bedzyk, *Small*, 2009, **5**, 750–757.
- B. L. Mojet, J. T. Miller, D. E. Ramaker and D. C. Koningsberger, *J. Catal.*, 1999, **186**, 373–386.
- I. E. Wachs, *Catal. Today*, 1996, **27**, 437–455.
- B. M. Weckhuysen and D. E. Keller, *Catal. Today*, 2003, **78**, 25–46.
- I. E. Wachs and C. A. Roberts, *Chem. Soc. Rev.*, 2010, **39**, 5002–5017.
- C. Y. Kim, J. W. Elam, M. J. Pellin, D. K. Goswami, S. T. Christensen, M. C. Hersam, P. C. Stair and M. J. Bedzyk, *J. Phys. Chem. B*, 2006, **110**, 12616–12620.
- O. Bondarchuk, X. Huang, J. Kim, B. D. Kay, L. S. Wang, J. M. White and Z. Dohnalek, *Angew. Chem., Int. Ed.*, 2006, **45**, 4786–4789.
- M. Baron, H. Abbott, O. Bondarchuk, D. Stacchiola, A. Uhl, S. Shaikhutdinov, H. J. Freund, C. Popa, M. V. Ganduglia-Pirovano and J. Sauer, *Angew. Chem., Int. Ed.*, 2009, **48**, 8006–8009.
- Z. Feng, C.-Y. Kim, J. W. Elam, Q. Ma, Z. Zhang and M. Bedzyk, *J. Am. Chem. Soc.*, 2009, **131**, 18200–18201.
- C. Y. Kim, A. A. Escudro, P. C. Stair and M. J. Bedzyk, *J. Phys. Chem. C*, 2007, **111**, 1874–1877.
- C. Y. Kim, J. A. Klug, P. C. Stair and M. J. Bedzyk, *J. Phys. Chem. C*, 2009, **113**, 1406–1410.
- Y. K. Kim, R. Rousseau, B. D. Kay, J. M. White and Z. Dohnalek, *J. Am. Chem. Soc.*, 2008, **130**, 5059–5061.
- M. E. McBriarty, M. J. Bedzyk and D. E. Ellis, *Surf. Sci.*, 2012, **606**, 1367–1381.
- J. Banas, M. Najbar and V. Tomasic, *Catal. Today*, 2008, **137**, 267–272.
- J. Banas, V. Tomasic, A. Weselucha-Birczynska and M. Najbar, *Catal. Today*, 2007, **119**, 199–203.
- E. Finocchio, M. Baldi, G. Busca, C. Pistarino, G. Romezzano, F. Bregani and G. P. Toledo, *Catal. Today*, 2000, **59**, 261–268.
- A. Satsuma, A. Hattori, K. Mizutani, A. Furuta, A. Miyamoto, T. Hattori and Y. Murakami, *J. Phys. Chem.*, 1988, **92**, 6052–6058.
- C. Schmitt, L. Giebeler, R. Schierholz, S. Endres, C. Fasel, H. Vogel and H. Fuess, *Z. Phys. Chem.*, 2007, **221**, 1525–1548.
- B. W. Batterman, *Phys. Rev.*, 1964, **133**, A759.
- P. L. Cowan, J. A. Golovchenko and M. F. Robbins, *Phys. Rev. Lett.*, 1980, **44**, 1680–1683.
- M. J. Bedzyk and L. Cheng, *Rev. Mineral. Geochem.*, 2002, **49**, 221–266.
- D. P. Woodruff, *Rep. Prog. Phys.*, 2005, **68**, 743–798.
- J. Zegenhagen, *Surf. Sci. Rep.*, 1993, **18**, 199–271.
- M. J. Bedzyk, in *Encyclopedia of Condensed Matter Physics*, ed. F. Bassani, G. J. Liedl and P. Wyder, Elsevier, Oxford, 2005, vol. 6, pp. 330–341.
- M. J. Bedzyk and G. Materlik, *Phys. Rev. B: Condens. Matter Mater. Phys.*, 1985, **31**, 4110–4112.
- N. Hertel, G. Materlik and J. Zegenhagen, *Z. Phys. B: Condens. Matter*, 1985, **58**, 199–204.
- L. Cheng, P. Fenter, M. J. Bedzyk and N. C. Sturchio, *Phys. Rev. Lett.*, 2003, **90**, 255503.
- Z. Zhang, P. Fenter, L. Cheng, N. C. Sturchio, M. J. Bedzyk, M. L. Machesky and D. J. Wesolowski, *Surf. Sci.*, 2004, **554**, L95–L100.
- J. S. Okasinski, C. Kim, D. A. Walko and M. J. Bedzyk, *Phys. Rev. B: Condens. Matter Mater. Phys.*, 2004, **69**, 041401.
- M. J. Bedzyk and P. Fenter, in *The X-Ray Standing Wave Technique: Principles and Applications*, ed. J. Zegenhagen and A. Kazimirov, World Scientific, Singapore, 2013, pp. xxii, 534 pp.
- Z. Feng, L. Cheng, C.-Y. Kim, J. W. Elam, Z. Zhang, L. A. Curtiss, P. Zapol and M. J. Bedzyk, *J. Phys. Chem. Lett.*, 2012, **3**, 2845–2850.
- Z. Feng, J. L. Lu, H. Feng, P. C. Stair, J. W. Elam and M. J. Bedzyk, *J. Phys. Chem. Lett.*, 2013, **4**, 285–291.
- C. Y. Kim, J. W. Elam, P. C. Stair and M. J. Bedzyk, *J. Phys. Chem. C*, 2010, **114**, 19723–19726.
- Z. Feng, A. Kazimirov and M. J. Bedzyk, *ACS Nano*, 2011, **5**, 9755–9760.
- V. Shapovalov and H. Metiu, *J. Phys. Chem. C*, 2007, **111**, 14179–14188.
- I. E. Wachs and B. M. Weckhuysen, *Appl. Catal., A*, 1997, **157**, 67–90.
- L. Salvati, L. E. Makovsky, J. M. Stencel, F. R. Brown and D. M. Hercules, *J. Phys. Chem.*, 1981, **85**, 3700–3707.
- D. C. Vermaire and P. C. Vanberge, *J. Catal.*, 1989, **116**, 309–317.
- C. Y. Kim, unpublished results, 2014.
- G. Silversmit, D. Depla, H. Poelman, G. B. Marin and R. De Gryse, *J. Electron Spectrosc. Relat. Phenom.*, 2004, **135**, 167–175.

- 47 J. N. Fiedor, A. Proctor, M. Houalla and D. M. Hercules, *Surf. Interface Anal.*, 1995, **23**, 204–212.
- 48 K. Senthil and K. Yong, *Nanotechnology*, 2007, **18**, 395604.
- 49 M. C. Marchi, S. A. Bilmes, C. T. M. Ribeiro, E. A. Ochoa, M. Kleinke and F. Alvarez, *J. Appl. Phys.*, 2010, **108**, 064912.
- 50 R. Lindsay, A. Wander, A. Ernst, B. Montanari, G. Thornton and N. M. Harrison, *Phys. Rev. Lett.*, 2005, **94**, 246102.
- 51 B. O. Loopstra and H. M. Rietveld, *Acta Crystallogr., Sect. B: Struct. Crystallogr. Cryst. Chem.*, 1969, **25**, 1420–1421.
- 52 R. Diehl, G. Brandt and E. Salje, *Acta Crystallogr., Sect. B: Struct. Crystallogr. Cryst. Chem.*, 1978, **34**, 1105–1111.
- 53 J. Kim, O. Bondarchuk, B. D. Kay, J. M. White and Z. Dohnalek, *Catal. Today*, 2007, **120**, 186–195.
- 54 C. Di Valentin, M. Rosa and G. Pacchioni, *J. Am. Chem. Soc.*, 2012, **134**, 14086–14098.
- 55 J. Nii, M. Wakihara and M. Taniguchi, *Mater. Res. Bull.*, 1979, **14**, 1069–1074.
- 56 A. F. Wells, *Structural Inorganic Chemistry*, Clarendon Press, Oxford, 1984.
- 57 Z. Wu, P. C. Stair, S. Rugmini and S. D. Jackson, *J. Phys. Chem. C*, 2007, **111**, 16460–16469.
- 58 D. P. Debecker, F. Bertinchamps, N. Blangenois, P. Eloy and E. M. Gaigneaux, *Appl. Catal., B*, 2007, **74**, 223–232.
- 59 D. P. Debecker, R. Delaigle, K. Bouchmella, P. Eloy, E. M. Gaigneaux and P. H. Mutin, *Catal. Today*, 2010, **157**, 125–130.
- 60 B. W. Lee, H. Cho and W. Shin, *J. Ceram. Process. Res.*, 2007, **8**, 203–207.
- 61 F. Bertinchamps, C. Gregoire and E. M. Gaigneaux, *Appl. Catal., B*, 2006, **66**, 10–22.
- 62 J. E. Herrera, J. H. Kwak, J. Z. Hu, Y. Wang, C. H. F. Peden, J. Macht and E. Iglesia, *J. Catal.*, 2006, **239**, 200–211.